

# Room-Temperature entangled quantum processor on integrated semiconductor photonics platform

Haibo Hu<sup>1,2,†</sup>, Yu Zhou<sup>1,†,\*</sup>, Ailun Yi<sup>3,4,†</sup>, Tongyuan Bao<sup>1</sup>, Chengying Liu<sup>1</sup>, Qi Luo<sup>1</sup>, Yao Zhang<sup>1</sup>, Zi Wang<sup>1</sup>, Zhengtong Liu<sup>2</sup>, Shuming Xiao<sup>1,2,5</sup>, Xin Ou<sup>3,4,\*</sup>, and Qinghai Song<sup>1,2,5\*</sup>

<sup>1</sup>Ministry of Industry and Information Technology Key Lab of Micro-Nano Optoelectronic Information System, Guangdong Provincial Key Laboratory of Semiconductor Optoelectronic Materials and Intelligent Photonic Systems, Harbin Institute of Technology, Shenzhen, 518055, China

<sup>2</sup>Pengcheng Laboratory, Shenzhen 518055, China

<sup>3</sup>State Key Laboratory of Functional Materials for Informatics, Shanghai Institute of Microsystem and Information Technology, Chinese Academy of Sciences, Shanghai 200050, China

<sup>4</sup>The Center of Materials Science and Optoelectronics Engineering, University of Chinese Academy of Sciences, Beijing 100049, China.

<sup>5</sup>Collaborative Innovation Center of Extreme Optics, Shanxi University, Taiyuan, Shanxi 030006, China

\*corresponding author(s): Yu Zhou(zhouyu2022@hit.edu.cn) or Xin Ou(ouxin@mail.sim.ac.cn) or Qinghai Song(qinghai.song@hit.edu.cn)

†these authors contributed equally to this work

## ABSTRACT

**The rise of the 4H-silicon-carbide-on-insulator (SiCOI) platform marks a promising pathway towards the realization of monolithic quantum photonic networks. However, the challenge of establishing room-temperature entangled registers on these integrated photonics platforms remains unresolved. Herein, we demonstrate the first entangled processor on the SiCOI platform. We show that both deterministic generation of single divacancy electron spins and near-unity spin initialization of a single <sup>13</sup>C nuclear spin can be achieved on SiCOI at room temperature. Besides coherently manipulating the single nuclear spin, a maximally entangled state with a fidelity of 0.89 has been prepared on this CMOS-compatible semiconductor-integrated photonics system. This work establishes the foundation for compact and on-chip solutions within existing defect-based computing and sensing protocols, positioning the SiCOI platform as the most promising candidate for integrated monolithic quantum photonic networks.**

## Introduction

The development of quantum networks with modular quantum nodes has ushered in a transformative era in distributed quantum computing, sensing, and communication<sup>1-4</sup>. Color centers in diamonds are at the forefront of constructing such quantum networks, taking two main approaches.<sup>5-12</sup> The first approach involves entanglement of nitrogen-vacancy centers in bulk diamonds at distant sites using herald protocols<sup>8</sup>. Recently, a more integrated quantum network node with silicon vacancy and proximal nuclear spin in diamond nanophotonics has been demonstrated<sup>11</sup>. However, these achievements have been heavily dependent on coupling emitted photons into optical fibers, resulting in considerable photon loss, degrading

system robustness and performance<sup>13</sup>. To further elevate the integration level and construct a monolithic quantum photonic network, integrating entangled quantum processors within thin films on insulators is essential—a feature currently absent in diamond photonics.

Silicon carbide, an emerging CMOS-compatible quantum material<sup>14–17</sup>, holds the potential to be the host for realizing a fully monolithic quantum photonic network processor<sup>2, 13</sup>. This potential is attributed to the recent rapid advancements in both SiC quantum registers and SiCOI platforms. On one hand, the coherence time of individual electron spins in SiC has significantly extended from milliseconds<sup>18</sup> to seconds<sup>19</sup>. Nuclear spins in SiC have been efficiently initialized through dynamical nuclear polarization (DNP)<sup>20</sup>. Furthermore, coherent control and entanglement of both ensemble<sup>21</sup> and individual nuclear spins<sup>22</sup> at cryogenic temperature provides a solid foundation for many quantum information applications<sup>23–30</sup>. On the other hand, the development of the quantum-grade SiCOI platform has opened up the possibility for on-chip photonics device integration. The SiCOI platforms have been shown to possess various functional possibilities, including photon frequency conversion to the telecom band<sup>31</sup>, generation of entangled photon pairs<sup>32</sup>, and electro-optic modulation<sup>33</sup>. However, despite the continuous breakthrough in SiC quantum registers and the platform, the integration of the two to a quantum photonics chip with entangled processors remains a significant challenge. We address this challenge and develop the first room-temperature entangled processor on the photonics-integrated platform. In detail, we have achieved deterministic generation of single divacancy spins on SiCOI and demonstrated near-unity initialization and coherent control of single <sup>13</sup>C nuclear spin. Furthermore, a maximally entangled state with a fidelity of 0.89 has been generated. These results signify a considerable advancement in realizing SiC-based quantum photonic networks.

## **Deterministic generation of single divacancy spins on SiCOI**

Figure 1a illustrates a SiC-based quantum photonic network comprising two main components: quantum registers and links. Establishing quantum links through SiC waveguides on insulators is not a formidable task, given the existing micro-fabrication techniques. However, three pivotal challenges related

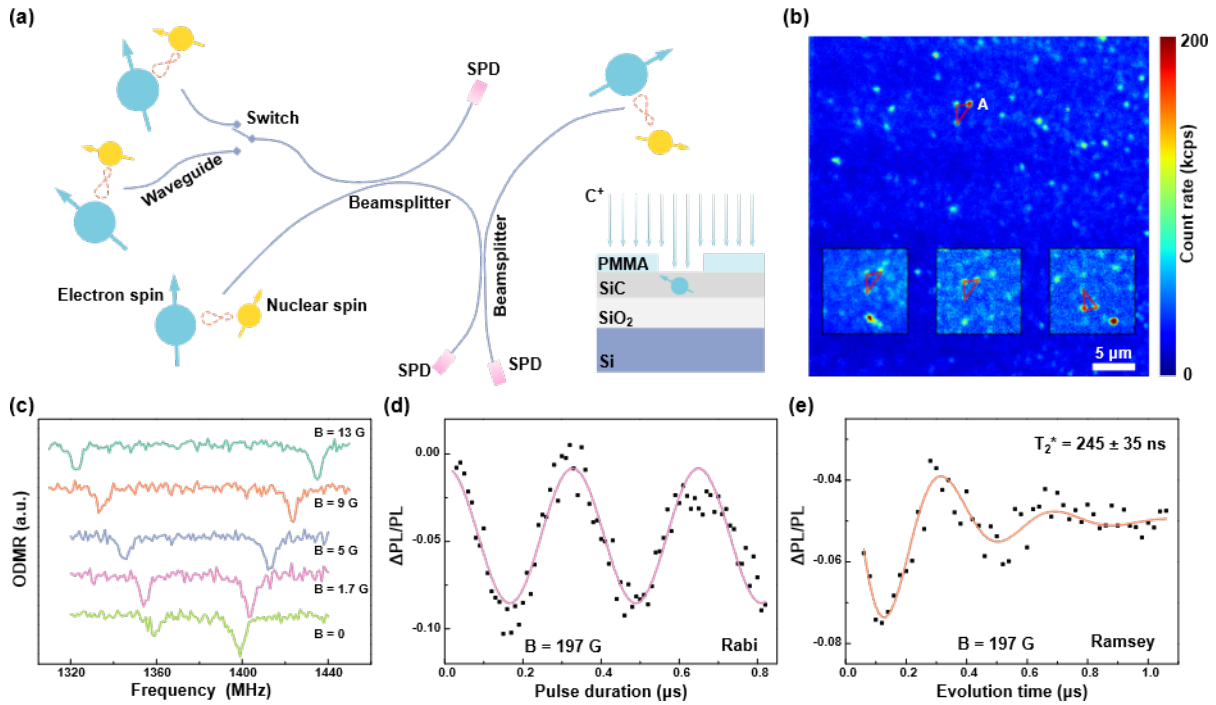


**Figure 1.** Generation and control of single PL6 on SiCOI. (a) Left: Defect-based quantum photonic network: a modular processor comprising optically addressable electron spins strongly coupled to nearby nuclear spins, connected by photons propagating in waveguides. Bottom right: cross-section of the SiCOI sample with 30 keV C<sup>+</sup> ion implantation through the 100 nm diameter PMMA hole array. (b) Confocal fluorescence image (40 × 40 μm<sup>2</sup>) of the implanted sample. The red triangles represent the evidence of implanted defect arrays in multiple regions. Point A corresponds to a single PL6 defect used in (c)-(e). (c) ODMR spectra of a single PL6 defect at different magnetic fields. (d) Rabi oscillation and (e) Ramsey oscillation of the single PL6 electron spin. The black dots represent the raw data, and the solid lines depict the fitting with the cosine function and cosine exponential decay function, respectively.

to the registers persist: the generation of single electron and nuclear spins, their efficient initialization, and the establishment of entanglement between them. First, we introduce the deterministic generation of single divacancy spins on SiCOI, which is a basic requirement for the integration of spin defects to scalable photonic devices on chip. A 4H-SiC wafer with an epitaxy layer is bonded to an oxidized Si wafer at room temperature. Subsequently, the bonded SiC layer is mechanically ground and then subjected to chemical-mechanical polished (CMP) to achieve a thickness of several micrometers. Next, the layer is etched with inductively coupled plasma to a thickness of around 200 nanometers (see Supplementary Notes for cross-section image). To generate single divacancy spins(Fig.1a), hole arrays are fabricated on the SiC layer using PMMA as a photoresist through E-beam lithography(inserted figure in Fig.1a). Following the 30 keV Carbon ion implantation with a dose of  $7.8 \times 10^{11} \text{ cm}^{-2}$ , the sample is annealed in a high

vacuum at 900 °C for 30 min to remove residual lattice damage. Figure 1b shows the room-temperature photo luminescence map of the implanted area using off-resonant excitation at 914 nm (refer to the Methods section for more details). Due to the low conversion yield, the defects generated through our ion implantation can be confirmed by the presence of red triangles in Fig.1b. The distance between two adjacent single defects is 2 micrometers, aligning with the spacing of PMMA hole array we designed. The conversion yield can be further improved by optimizing the implantation dose in the future. Those surrounding randomly distributed emissions are from intrinsic emitters that existed before our implantation. To confirm the defect we generate is PL6 (a recently reported SiC divacancy spin with high brightness and ODMR contrast<sup>34</sup>), we perform optical detected magnetic resonance(ODMR) of defect A at various B fields, with the magnetic field arranged parallel to the c-axis. The two branches of the OMDR spectrum diverge with a slope of 2.8 MHz per gauss, as shown in Figure 1c. Together with the zero-field splitting parameters  $D = 1378.9$  MHz,  $E = 19.7$  MHz, 150 Kcps saturation intensity (Supplementary Notes), and  $\sim 15\%$  ODMR contrast, all these characteristics are consistent with PL6<sup>34</sup>. The small discrepancies between the D and E with the literature are attributed to the lateral and longitudinal strain of the thin film<sup>35</sup>. Subsequently, we demonstrate coherent control of the single PL6 electron spin, as evidenced by the Rabi oscillation and Ramsey fringes displayed in Figure 1d and 1e, respectively. From the fitting, the inhomogeneous spin-dephasing time  $T_2^*$  is extracted to be  $245 \pm 35$  ns. The longitudinal relaxation time  $T_1$  is measured to be  $219 \mu\text{s}$  (Supplementary Notes), similar to those in bulk materials<sup>34</sup>. This indicates that the previous fabrication process doesn't degrade the electron spin properties.

### **Coherent control of single nuclear spins on SiCOI**

Having demonstrated deterministic implantation and coherent control of single PL6 spin, we proceed to nuclear spin manipulation and initialization. In natural SiC, approximately 1.1% of the carbon atoms (<sup>13</sup>C) and 4.7% of silicon atoms <sup>29</sup>Si possess nuclear spins with  $I = 1/2$ . Strong coupling occurs when the nuclear spin resides within several lattice sites of PL6. The hyperfine interaction can well exceed both the electron and nuclear spin dephasing rates  $1/T_2^*$ . This strong coupling is valuable for implementing fast gate operations and high-speed quantum memories<sup>36,37</sup>. We successfully identified an electron-nuclear spin-coupled system in the sample, as shown in Figure 2A. The single PL6 electron spin is strongly

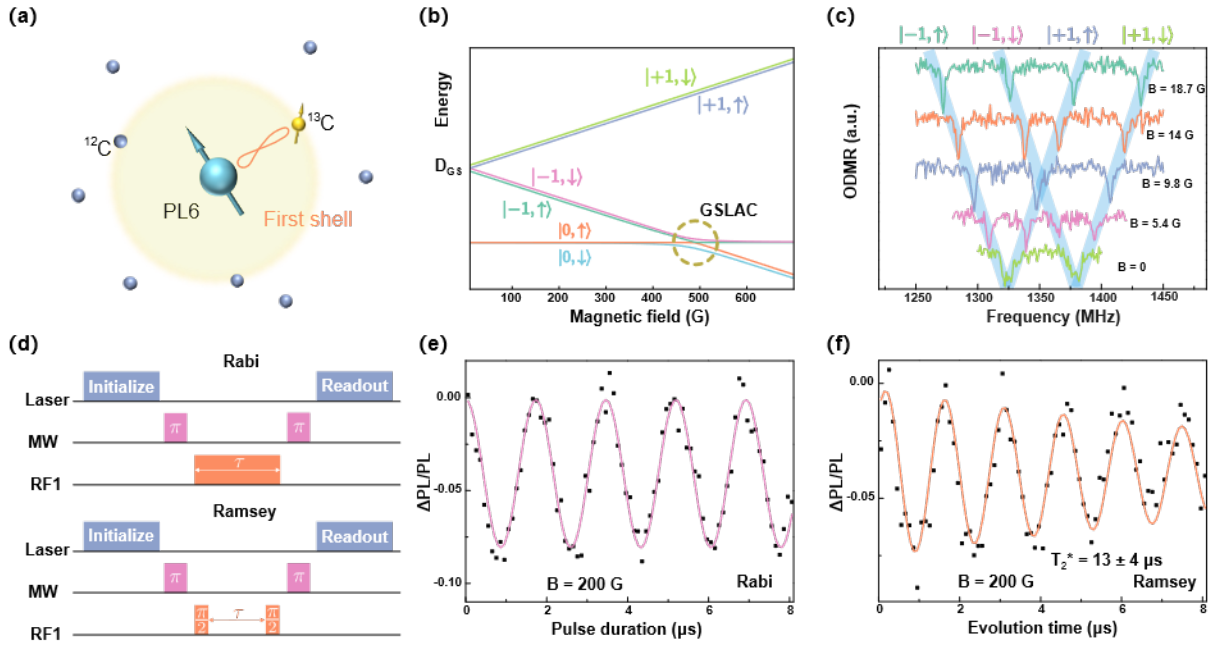


**Figure 2.** Coherent control of single nuclear spins on SiCOI. (a) An illustration of a single PL6 electron spin with a  $^{13}\text{C}$  nuclear spin in the first shell. (b) The energy diagram of ground state spin sublevels as a function of c-axis magnetic field  $B$ . GSLAC is marked with a dashed circle. (c) ODMR spectra of the single PL6 electron spin coupled with the first-shell  $^{13}\text{C}$  nuclear spin in different magnetic fields. The pale blue lines indicate the change of different peaks with the magnetic field. The slope is 2.8 MHz/G, corresponding to a c-axis defect's Zeeman splitting. (d) Nuclear Rabi oscillation and Ramsey fringes pulse sequences containing laser initialize, MW1  $\pi$ -pulse and RF  $\pi$ -pulse or  $\pi/2$ -pulse. MW1 and RF are the pulses that drive  $|0, \uparrow\rangle$  to  $|-1, \uparrow\rangle$  and  $|-1, \uparrow\rangle$  and  $|-1, \downarrow\rangle$  respectively. The nuclear is mapped and readout out through the electron spin. (e) Rabi and (f) Ramsey of the  $^{13}\text{C}$  nuclear spin. The Ramsey fringe is fitted with a cosine exponential decay function, yielding a  $T_2^* = 13 \pm 4 \mu\text{s}$ .

coupled to a first shell  $^{13}\text{C}$  nuclear spin<sup>36</sup>. We use 0,  $\pm 1$  and  $\uparrow, \downarrow$  to denote the electron and nuclear spin respectively. The full Hamiltonian of the system can be written as

$$H = D[S_z^2 - S(S+1)/3] + \gamma_e B \cdot S + S \cdot A \cdot I - \gamma_{^{13}\text{C}} B \cdot I \quad (1)$$

Here,  $D$  represents the zero-field splitting parameter of the electron spin,  $S$  and  $I$  are the electron spin-1 and nuclear spin-1/2 operators, respectively.  $\gamma_e = 2.8 \text{ GHz T}^{-1}$  is the electron-spin gyromagnetic ratio.  $\gamma_{^{13}\text{C}} = 10.708 \text{ MHz T}^{-1}$  is the gyromagnetic ratio of  $^{13}\text{C}$  nuclear spin.  $A$  is the hyperfine-interaction tensor between PL6 and  $^{13}\text{C}$ . When the nuclear spin resides in the first shell, the electron-nuclear spin coupling is strong enough to split the ground state energy levels. Two individually addressable separated around 55.1 MHz correspond to nuclear spin  $\uparrow, \downarrow$  respectively at zero  $B$  field. Depending on their position in the lattice,

the hyperfine interaction strength varies drastically; We attribute this huge hyperfine splitting to coupling with a carbon isotope nuclear spin  $^{13}\text{C}$  in the first shell<sup>38</sup>. When a c-axis magnetic field is added,  $m_s \pm 1$  are no longer degenerate and split at a slope of 2.8 MHz/G due to Zeeman splitting, as shown in Figures 2b and 2c. The ground-state spin-level anticrossings (GSLAC) region is marked with a dashed circle. We choose a B field 200G between the GSLAC and zero fields to resolve the four transitions well and far away from anticrossing to perform the coherent control. At this B field, there is no nuclear spin polarization, so the nuclear spin must be mapped to the electron spin before control and readout, as the control sequence depicted in Figure 2d. The frequency of RF corresponds to the energy gap between  $|-1, \uparrow\rangle$  and  $|-1, \downarrow\rangle$ . We prepare the electron spin in the  $m_s = -1$  state and use the RF pulse to drive nuclear Rabi oscillations (Figure 2d) and Ramsey fringes (Figure 2e). The Ramsey fringes yield a pure dephasing time of  $13 \pm 4 \mu\text{s}$ . The relatively short time scale is due to the strong interaction with the environment through the electron spin<sup>39</sup>. It can be significantly improved by choosing a nuclear spin not in the first shell<sup>22</sup> or decoupling the electron spin with the help of the ionization process<sup>40</sup>.

### Near-unity Dynamic Polarization of Single Nuclear Spins on SiCOI

Besides coherent control, efficient initialization of the single nuclear spin memory is another critical capability in quantum information processing. DNP can effectively transfer electron spins to neighboring nuclei via hyperfine interaction, serving as a basis for quantum memories and computing<sup>40,41</sup>, nuclear magnetic resonance sensitivity enhancement<sup>42</sup>, and solid-state nuclear gyroscopes<sup>27</sup>. We demonstrate that room-temperature DNP can be efficiently utilized in an integrated photonic platform, achieving a near-unity degree of polarization for a single nuclear spin. When the system is far from the anti-crossing point, nuclear spins will not be optically polarized, and equal populations of  $|\pm 1, \uparrow\rangle$  and  $|\pm 1, \downarrow\rangle$  will result in the same intensity of the ODMR spectrum, as shown in Figure 2c. Near GSLAC, in each optical cycle,  $|0, \downarrow\rangle$  may evolve into  $|-1, \uparrow\rangle$ , exchanging electron and nuclear polarizations. And subsequent optical cycles polarize  $|-1, \uparrow\rangle$  to  $|0, \uparrow\rangle$ , the whole process polarizes the nuclear spins simply by optical illumination<sup>20,43</sup>. To uncover the detailed mechanism, we performed ODMR measurements at different

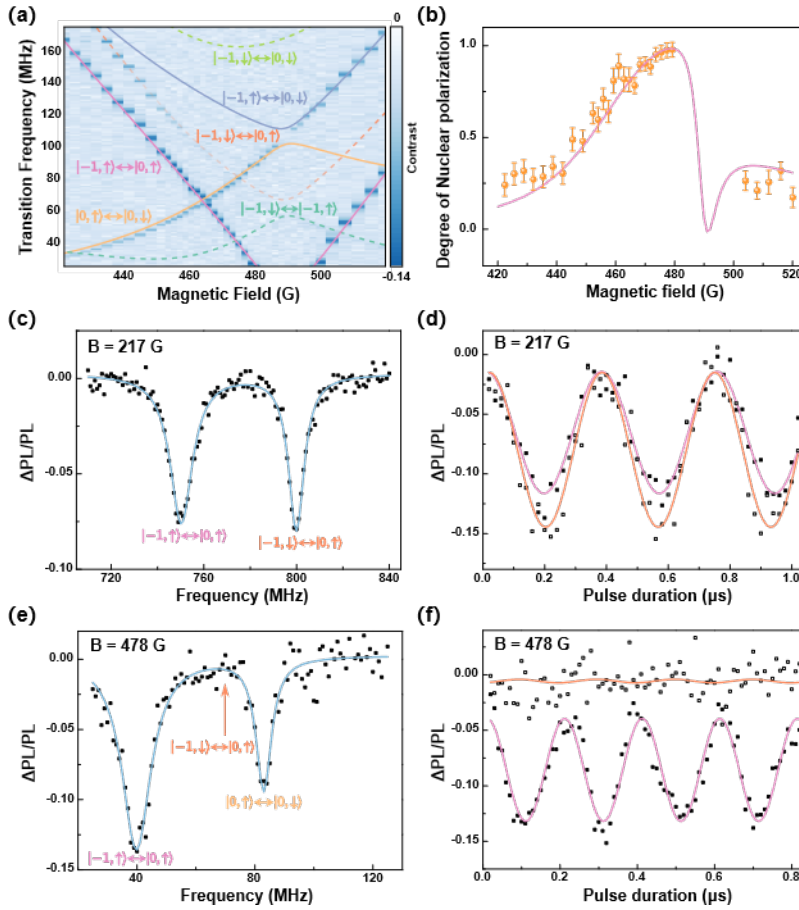


**Figure 3.** Dynamic polarization of single nuclear spin on SiCOI. (a) ODMR spectra of the single PL6 defect coupled with single first-shell  $^{13}\text{C}$  nuclear spin at different magnetic fields near GSLAC. The vibrant lines are the theoretical calculation of the transition frequency of the spin sublevels with the total Hamiltonian 1. (b) The degree of nuclear spin polarization is defined by  $P = (I^+ - I^-)/(I^+ + I^-)$ , and  $I^+$  and  $I^-$  are extracted from the Lorentzian fitting of the ODMR spectra in a. The maximum polarization degree is  $0.98 \pm 0.04$ . (c) and (e) ODMR spectra recorded for  $B = 217$  G (non-polarization) and  $B = 478$  G (polarization). The peaks correspond to transitions  $|-1, \uparrow\rangle \leftrightarrow |0, \uparrow\rangle$  and  $|-1, \downarrow\rangle \leftrightarrow |0, \uparrow\rangle$  respectively. (d)&(f) Rabi oscillations of the transitions in (c)&(e).

magnetic fields near GSLAC, as illustrated in Figure 3a. Our microwave source limits the lower bound of the microwave frequency to 20 MHz. Once the hyperfine tensor  $A$  is given, the energy separation between the electron and nuclear eigenstates can be calculated from the total Hamiltonian<sup>37,44</sup>. We present an example that best fits the experiment results with colored solid lines (with  $A_{xx} = A_{yy} = 93.1$  MHz,  $A_{zz} = 56.5$  MHz), where each color line represents a transition. Notably,  $|-1, \uparrow\rangle$  to  $|0, \uparrow\rangle$  maintains its intensity as the magnetic field approaches the anti-crossing point. In contrast,  $|-1, \downarrow\rangle$  to  $|0, \uparrow\rangle$  weakens and vanishes from  $B = 460$  G, signifying strong nuclear polarization occurs. We define the degree of nuclear spin polarization  $P$  as  $(I^+ - I^-)/(I^+ + I^-)$ , where  $I^+$  and  $I^-$  denote the populations of the nuclear spins

$\uparrow$  and  $\downarrow$  respectively<sup>20,43</sup>. The populations are quantified by performing the Lorentzian fit of individual peaks. As illustrated in Figure.3b, the solid lines are the theoretically calculated curve of  $\rho = \rho_{\uparrow} - \rho_{\downarrow}$  ( $\rho_{\uparrow}$  and  $\rho_{\downarrow}$  are the populations of nuclear spin up and down, see Methods). The maximum polarization degree we achieved is  $0.98 \pm 0.04$ , reaching near-unity initialization of the single nuclear spin. To confirm this polarization, we compare the ODMR spectra and Rabi oscillations at two magnitudes of a magnetic field applied along the c-axis of the sample, as represented in Figure 3c-e. When  $B = 217$  G, the two ODMR spectra have similar contrast (Figure 3c), the same as in rabi oscillations(Figure 3d). However, when  $B = 478$ G,  $|-1, \downarrow\rangle$  to  $|0, \uparrow\rangle$  vanishes in both ODMR spectra and corresponding Rabi nutation (Figure 3e and 3f).

### **Optical nuclear magnetic resonance (ONDMR) and the entanglement generation on SiCOI**

After performing full control and near-unity polarization of a single nuclear spin, we have all the prerequisites to demonstrate the generation of an electron-nuclear entangled state on this photonics-integrated semiconductor platform. The simplified energy level scheme of the electron-nuclear coupled system is depicted in Figure 4a. MW and RF2 in this subspace can be obtained directly from the ODMR measurements in the previous section, while RF1 is missing due to the strong nuclear polarization near GSLAC. To recover RF1, the pulse sequence in Figure 4b is used. After the system is optically initialized to  $|-1, \uparrow\rangle$ , we prepare the electron spin in the  $m_s = -1$  state and then apply an RF pulse. The state is then read out by projecting onto the electron spin again. By varying the frequency of the RF pulse, we obtain the optically nuclear magnetic resonance (ONDMR) spectra, as indicated in Figure 4b. After successfully addressing all three transitions, we can perform quantum state tomography (QST) utilizing MW1 as a working transition(see Supplementary Notes for details). We track the evolution of electron-nuclear states by performing quantum state tomography at two stages. First, the qubits are initialized by optical pumping only, after which we perform quantum state tomography. The measured density matrix is presented below the circuit in Figure 4b with a fidelity of 0.98. This fidelity agrees well with the degree of polarization we obtained with the ODMR fitting method before. Then, we create a maximal superposition by applying

two gates, as presented in Figure 4d, so that the two-qubit is maximum entangled to one of the Bell states  $|\Psi^+\rangle = (|0, \uparrow\rangle + |-1, \downarrow\rangle)/\sqrt{2}$  (Figure 4d). We generate the entanglement in this system with a fidelity of 0.89, estimated with the density matrix from the quantum state tomography.

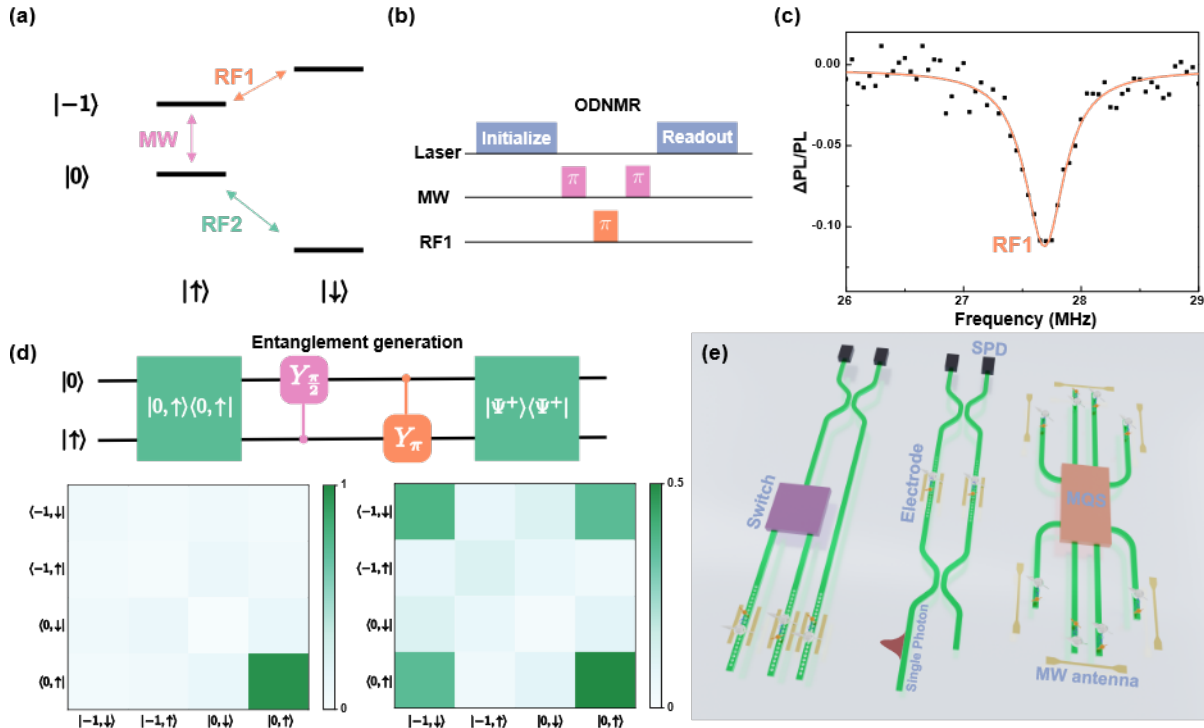


**Figure 4.** Entanglement generation and quantum state tomography. (a) Simplified energy level scheme of the electron-nuclear coupled system. MW, RF1, and RF2 are three addressable transitions. MW and RF2 can be obtained directly from the ODMR spectra, while RF1 is missing due to the strong nuclear polarization. To recover RF, the pulse sequence in (b) is used with the help of electron spin. (c) Optical nuclear magnetic resonance measurement with the sequence in b. (d) upper panel: quantum circuit diagram for the entanglement generation and state tomography. lower panel: density matrix from quantum state tomography of the initial  $(|0, \uparrow\rangle \langle 0, \uparrow|)$  and entangled state  $(|\Psi^+\rangle \langle \Psi^+|)$ . The fidelity of the target state is 0.98 and 0.89, respectively. (e) A conceptual diagram for three representative quantum photonic chip configurations on the 4H-SiCOI platform. Left: distributed photonic architecture aimed at remote entanglement generation utilizing a heralded protocol<sup>5</sup>. Central: distributed photonic architecture aimed at scalable quantum information processing proposed in ref<sup>3</sup>. right panel: distributed quantum sensing architecture, leveraging multi-node simultaneous sensing or high-fidelity entanglement-enhanced sensing to surpass the standard quantum limit in measurement sensitivity<sup>41,45,46</sup>.

## Conclusion

SiCOI stands out for developing wafer-scale monolithic quantum photonic network processors with on-chip quantum nodes and channels. Our work marks a pivotal step towards achieving this goal. We

have successfully demonstrated the deterministic generation of single divacancy spins on SiCOI without degrading the spin performance. Impressively, using dynamical optical pumping near GSLAC, we have achieved a high degree of single nuclear spin polarization, reaching nearly 98% at ambient conditions. Moreover, we have coherently controlled a single nuclear spin and generated a maximally entangled state with a fidelity of 0.89 on this integrated semiconductor photonic platform.

This work lays a foundation for compact and on-chip solutions of existing defect-based sensing protocols, such as atomic nuclear spin imaging<sup>26</sup>, nuclear spin gyroscope<sup>27,28</sup>, error correction assist sensing<sup>29,30</sup>, etc. More importantly, these results hold exciting implications for various modular applications, such as distributed quantum communication, computing, and sensing, as visualized in Figure 4e. The electron-nuclear entangled processor is a building block in these possible configurations, providing long-lived nuclear spin memories for quantum information storage and processing. In the case of remote entanglement generation, a photonic crystal cavity is integrated with each processor to enhance the spin-photon interaction. The microwave antenna and electrodes are fabricated on the chip for the spin or charge control and Stack-shift tuning<sup>47</sup>. Among the three representative chip configurations, the leftmost design utilizes a heralded protocol<sup>5</sup> to generate remote entanglement. Spin-entangled photons from different processors on the chip interfere on a 50:50 beam splitter and are then detected using waveguide-integrated superconducting nanowire single-photon detectors<sup>47</sup>. The central design outlines a distributed photonic architecture aimed at scalable quantum information processing, as proposed before<sup>3</sup>. Modules are connected by photons propagating in waveguides, collectively used to generate a cluster state of nuclear spins. The rightmost design represents a distributed quantum sensing chip, leveraging multi-node simultaneous sensing<sup>41</sup> or high-fidelity entanglement-enhanced sensing to surpass the standard quantum limit<sup>45,46</sup> in measurement sensitivities. The sample we used are primitive commercial wafer, the coherence time can be greatly improved further by reducing the temperature<sup>14</sup> and isotope purification<sup>22</sup>.

## Methods

**4H-SiCOI fabrication.** 4-inch 4H-SiC wafer with epitaxy layer and the oxidized Si substrate were activated by O<sub>2</sub>/N<sub>2</sub> plasma, and then the two wafers were directly bonded at room temperature. The bonded wafer was annealed at 400 °C to enhance the bonding strength. After annealing treatment,

the thickness of the bonded SiC layer was reduced from 500  $\mu\text{m}$  to sub 10  $\mu\text{m}$  by the mechanical grinding process. The grinding process involves a diamond-resin bonded wheel to remove the SiC layer mechanically. Then, the wafer was cut into 10 mm  $\times$  12 mm dies, and each die was further thinned down to the desired thickness by inductively-coupled-plasma (ICP) reactive ion etching (RIE) with  $\text{SF}_6/\text{O}_2$  plasma. To fabricate single divacancy spins, hole arrays are patterned on the SiC layer using PMMA as a photoresist through E-beam lithography. Following the 30 keV Carbon ion implantation with a dose of  $7.8 \times 10^{11} \text{ cm}^{-2}$ , the sample is annealed in a high vacuum at 900  $^\circ\text{C}$  for 30 min to remove residual lattice damage.

**Confocal scan and spin manipulation.** Single defects are characterized by a home-built confocal microscope operating at room temperature. A 914 nm excitation laser is focused on the single defect through a Nikon high numerical aperture oil objective (Nikon, CFI Plan Fluor 100X Oil). The fluorescence is finally counted by a superconducting nanowire single photon detector (SNSPD, Photon Technology) after passing a dichroic mirror (Semrock, Di02-R980-25 $\times$ 36) and a 1000 nm long-pass filter (Thorlabs, FELH1000). For the ODMR, Rabi, and Ramsey measurements, the microwave was generated using a synthesized signal generator (Mini-Circuits, SSG-6000 RC) and then gated by a switch (Mini-Circuits, ZASWA-2-50DR+). After amplification (Mini-Circuits, ZHL-25W-272+), the microwave signals were fed to a 20- $\mu\text{m}$ -wide copper wire above the sample's surface. The excitation laser was modulated using an acoustic-optic modulator. The timing sequence of the electrical signals for manipulating and synchronizing the laser, microwave, and counter was generated using a pulse generator (SpinCore, PBESRPRO500). The external magnetic field is applied with a permanent magnet along the 4H-SiC c axis. Otherwise, the large transverse magnetic field may obscure the effect of the off-diagonal hyperfine elements. The strength of the magnetic field is adjusted by the distance of the magnet from the laser focus point on the sample. The magnetic field is determined precisely using ODMR spectrums from a single PL6 electron spin as a magnetometer.

**Probability of electron-nuclear spin flip-flop.** The nuclear polarization  $P$  is related to the probability of electron-nuclear spin flip-flop, which can be calculated by the degree of mixing between spin eigenstates and energy eigenstates. In our work, the probability of nuclear spin up ( $\rho_\uparrow$ ) and down ( $\rho_\downarrow$ ) flips are calculated by relevant eigenstates<sup>37</sup>:

$$\rho_{\uparrow} = 4 \cdot |\langle 0, \downarrow | \beta \rangle|^2 \cdot \left[ |\langle 0, \downarrow | \chi \rangle|^2 + |\langle 0, \downarrow | \delta \rangle|^2 \right] + 4 \cdot |\langle 0, \downarrow | \delta \rangle|^2 \cdot \left[ |\langle 0, \downarrow | \alpha \rangle|^2 + |\langle 0, \downarrow | \chi \rangle|^2 \right]$$

$$\rho_{\downarrow} = 4 \cdot |\langle 0, \uparrow | \alpha \rangle|^2 \cdot \left[ |\langle 0, \uparrow | \chi \rangle|^2 + |\langle 0, \uparrow | \delta \rangle|^2 \right] + 4 \cdot |\langle 0, \uparrow | \chi \rangle|^2 \cdot \left[ |\langle 0, \uparrow | \beta \rangle|^2 + |\langle 0, \uparrow | \delta \rangle|^2 \right]$$

where  $|\alpha\rangle, |\beta\rangle, |\chi\rangle$  and  $|\delta\rangle$  are the eigenstates of Hamiltonian. The projections onto the  $|0, \uparrow / \downarrow\rangle$  states of these eigenstates are affected by the off-diagonal hyperfine elements.

**Entanglement fidelity.** To determine the entanglement fidelity, we compare the measured density matrix  $\rho$  with the ideal target density matrix  $\rho'$  using the following definition<sup>22</sup>:

$$F = \text{Tr}(\sqrt{\sqrt{\rho}\rho'\sqrt{\rho}})$$

## References

1. Kimble, H. J. The quantum internet. *Nature* **453**, 1023–1030 (2008).
2. Awschalom, D. *et al.* Development of quantum interconnects (quics) for next-generation information technologies. *PRX Quantum* **2**, 017002 (2021).
3. Nemoto, K. *et al.* Photonic architecture for scalable quantum information processing in diamond. *Phys. Rev. X* **4**, 031022 (2014).
4. Hucul, D. *et al.* Modular entanglement of atomic qubits using photons and phonons. *Nat. Phys.* **11**, 37–42 (2015).
5. Bernien, H. *et al.* Heralded entanglement between solid-state qubits separated by three metres. *Nature* **497**, 86–90 (2013).
6. Hensen, B. *et al.* Loophole-free bell inequality violation using electron spins separated by 1.3 kilometres. *Nature* **526**, 682–686 (2015).
7. Hermans, S. *et al.* Qubit teleportation between non-neighbouring nodes in a quantum network. *Nature* **605**, 663–668 (2022).
8. Pompili, M. *et al.* Realization of a multinode quantum network of remote solid-state qubits. *Science* **372**, 259–264 (2021).
9. Sipahigil, A. *et al.* An integrated diamond nanophotonics platform for quantum-optical networks. *Science* **354**, 847–850 (2016).

10. Nguyen, C. *et al.* Quantum network nodes based on diamond qubits with an efficient nanophotonic interface. *Phys. Rev. Lett.* **123**, 183602 (2019).
11. Stas, P.-J. *et al.* Robust multi-qubit quantum network node with integrated error detection. *Science* **378**, 557–560 (2022).
12. Bersin, E. *et al.* Development of a boston-area 50-km fiber quantum network testbed. *arXiv preprint arXiv:2307.15696* (2023).
13. Lukin, D. M., Guidry, M. A. & Vučković, J. Integrated quantum photonics with silicon carbide: challenges and prospects. *PRX Quantum* **1**, 020102 (2020).
14. Falk, A. L. *et al.* Polytype control of spin qubits in silicon carbide. *Nat. Commun.* **4**, 1819 (2013).
15. Widmann, M. *et al.* Coherent control of single spins in silicon carbide at room temperature. *Nat. Mater.* **14**, 164–168 (2015).
16. Wang, J. *et al.* Bright room temperature single photon source at telecom range in cubic silicon carbide. *Nat. Commun.* **9**, 4106 (2018).
17. Wang, J.-F. *et al.* Coherent control of nitrogen-vacancy center spins in silicon carbide at room temperature. *Phys. Rev. Lett.* **124**, 223601 (2020).
18. Christle, D. J. *et al.* Isolated electron spins in silicon carbide with millisecond coherence times. *Nat. materials* **14**, 160–163 (2015).
19. Anderson, C. P. *et al.* Five-second coherence of a single spin with single-shot readout in silicon carbide. *Sci. Adv.* **8**, eabm5912 (2022).
20. Falk, A. L. *et al.* Optical polarization of nuclear spins in silicon carbide. *Phys. Rev. Lett.* **114**, 247603 (2015).
21. Klimov, P. V., Falk, A. L., Christle, D. J., Dobrovitski, V. V. & Awschalom, D. D. Quantum entanglement at ambient conditions in a macroscopic solid-state spin ensemble. *Sci. Adv.* **1**, e1501015 (2015).
22. Bourassa, A. *et al.* Entanglement and control of single nuclear spins in isotopically engineered silicon carbide. *Nat. Mater.* **19**, 1319–1325 (2020).

23. Taminiou, T. H., Cramer, J., van der Sar, T., Dobrovitski, V. V. & Hanson, R. Universal control and error correction in multi-qubit spin registers in diamond. *Nat. Nanotechnol.* **9**, 171–176 (2014).
24. Waldherr, G. *et al.* Quantum error correction in a solid-state hybrid spin register. *Nature* **506**, 204–207 (2014).
25. Zaiser, S. *et al.* Enhancing quantum sensing sensitivity by a quantum memory. *Nat. Commun.* **7**, 12279 (2016).
26. Ajoy, A., Bissbort, U., Lukin, M. D., Walsworth, R. L. & Cappellaro, P. Atomic-scale nuclear spin imaging using quantum-assisted sensors in diamond. *Phys. Rev. X* **5**, 011001 (2015).
27. Jarmola, A. *et al.* Demonstration of diamond nuclear spin gyroscope. *Sci. Adv.* **7**, eabl3840 (2021).
28. Soshenko, V. V. *et al.* Nuclear spin gyroscope based on the nitrogen vacancy center in diamond. *Phys. Rev. Lett.* **126**, 197702 (2021).
29. Arrad, G., Vinkler, Y., Aharonov, D. & Retzker, A. Increasing sensing resolution with error correction. *Phys. Rev. Lett.* **112**, 150801 (2014).
30. Hirose, M. & Cappellaro, P. Coherent feedback control of a single qubit in diamond. *Nature* **532**, 77–80 (2016).
31. Lukin, D. M. *et al.* 4h-silicon-carbide-on-insulator for integrated quantum and nonlinear photonics. *Nat. Photonics* **14**, 330–334 (2020).
32. Guidry, M. A., Lukin, D. M., Yang, K. Y., Trivedi, R. & Vučković, J. Quantum optics of soliton microcombs. *Nat. Photonics* **16**, 52–58 (2022).
33. Powell, K. *et al.* Integrated silicon carbide electro-optic modulator. *Nat. Commun.* **13**, 1851 (2022).
34. Li, Q. *et al.* Room-temperature coherent manipulation of single-spin qubits in silicon carbide with a high readout contrast. *Natl. Sci. Rev.* **9**, nwab122 (2022).
35. Falk, A. L. *et al.* Electrically and mechanically tunable electron spins in silicon carbide color centers. *Phys. Rev. Lett.* **112**, 187601 (2014).
36. Rao, K. R. K. & Suter, D. Characterization of hyperfine interaction between an nv electron spin and a first-shell c 13 nuclear spin in diamond. *Phys. Rev. B* **94**, 060101 (2016).

37. Wang, H.-J. *et al.* Sensitive magnetic control of ensemble nuclear spin hyperpolarization in diamond. *Nat. Commun.* **4**, 1940 (2013).
38. Son, N. *et al.* Divacancy in 4h-sic. *Phys. Rev. Lett.* **96**, 055501 (2006).
39. Mizuochi, N. *et al.* Coherence of single spins coupled to a nuclear spin bath of varying density. *Phys. Rev. B* **80**, 041201 (2009).
40. Dutt, M. G. *et al.* Quantum register based on individual electronic and nuclear spin qubits in diamond. *Science* **316**, 1312–1316 (2007).
41. Cai, M. *et al.* Parallel optically detected magnetic resonance spectrometer for dozens of single nitrogen-vacancy centers using laser-spot lattice. *Rev. Sci. Instruments* **92** (2021).
42. Giovannetti, V., Lloyd, S. & Maccone, L. Advances in quantum metrology. *Nat. Photonics* **5**, 222–229 (2011).
43. Jacques, V. *et al.* Dynamic polarization of single nuclear spins by optical pumping of nitrogen-vacancy color centers in diamond at room temperature. *Phys. Rev. Lett.* **102**, 057403 (2009).
44. Ivády, V. *et al.* Theoretical model of dynamic spin polarization of nuclei coupled to paramagnetic point defects in diamond and silicon carbide. *Phys. Rev. B* **92**, 115206 (2015).
45. Proctor, T. J., Knott, P. A. & Dunningham, J. A. Multiparameter estimation in networked quantum sensors. *Phys. Rev. Lett.* **120**, 080501 (2018).
46. Komar, P. *et al.* A quantum network of clocks. *Nat. Phys.* **10**, 582–587 (2014).
47. Anderson, C. P. *et al.* Electrical and optical control of single spins integrated in scalable semiconductor devices. *Science* **366**, 1225–1230 (2019).

## Acknowledgments

We acknowledge the support from National Key R&D Program of China (Grant No. 2021YFA1400802, 2022YFA1404601), the National Natural Science Foundation of China (Grant No. 12304568, 11934012, 62293520, 62293522, 62293521, 12074400 and 62205363), the GuangDong Basic and Applied Basic Research Foundation (Grant No. 2022A1515110382), Young Elite Scientists Sponsorship Program by

CAST, New Cornerstone Science Foundation through the XPLOER PRIZE, Shanghai Science and Technology Innovation Action Plan Program (Grant No. 22JC1403300), CAS Project for Young Scientists in Basic Research (Grant No. YSBR-69).

## **Author contributions**

Y.Z., S.X., and Q.S. conceived the idea. A.Y. and X.O. prepared the SiCOI sample. H.H., Y.Z., and Z.W. carried out the EBL lithography and SiC defect generation. Y.Z. and H.H. built the setup and carried out the measurements. H.H., T.B., Y.Z., and Q.S. performed the simulations. Y.Z. and H.H. wrote the manuscript. All authors contributed to analyzing the data and commenting on the manuscript.

## **Data availability.**

Source data to generate figures and tables are available from the corresponding authors.

## **Competing interests**

The authors declare no competing interests.